Experimental and Numerical Analysis of Skin-Stiffener Separation Using a Seven-Point Bend Configuration

Cyrus J. R. Kosztowny,[1] Carlos G. Dávila,[2] Kyongchan Song,[3] Cheryl A. Rose,[2] and Wade Jackson[2]
NASA Langley Research Center, Hampton, VA, 23681

Skin-stiffener separation in stiffened composite panels consists of a complex interaction between multiple scales of progressive damage and failure mechanisms. This work used a superposed cohesive element method of modeling resistance curve effects that represents the structural interface of a unidirectional tape skin and a fabric stiffener. Finite element models using cohesive elements with input properties obtained from tape-to-fabric interface characterization tests were compared to experimental results of a stable skin-stiffener separation characterization test using a seven-point bend fixture. This fixture deformed the stiffened panel specimens into a buckled configuration which induced mixed-mode interlaminar stress states at the skin-stiffener interface. The advantage of this fixture was the potential for more stable damage initiation and delamination growth compared to a stringer-stiffened panel under axial compression. Use of the superposed cohesive elements showed promise, but the characterization of interface material properties as input to the cohesive elements remains a crucial component to be investigated to ensure accurate prediction of skin-stiffener separation.

I. Introduction

Advanced carbon fiber reinforced polymer (CFRP) composite structural panels continue to have increased use as primary structures in aerospace applications. The prediction of structural failure of CFRP stiffened panels has been shown to be a challenge as failure modes often interact under complex stress states as damage progresses. Skin-stiffener separation, in particular, has been an area of significant research interest to the aerospace community. As a stiffener separates from the skin, the loss of load-carrying capability becomes significant. In a skin-stiffener separation event, matrix microcracking, delamination migration, multiple delamination initiation locations, and fiber failure[1] may all occur. Widespread adoption of advanced carbon fiber reinforced polymer composites in stiffened structures warrants continued research into understanding the underlying fundamental mechanisms during failure events such as skin-stiffener separation. Concurrently, application of engineering tools, based on these fundamental mechanisms, to capture stiffened panel response and separation behavior with appropriate fidelity is desirable. There is a trade-off between features such as fidelity – or the capability of the model to capture specific physical phenomena such as matrix microcracking, accuracy – or how well numerical results agree with experimentally obtained data for a given level of fidelity, computational efficiency, and required user proficiency[2] often with the designer or stress analyst settling for only one or two features for a particular task.

Cohesive elements are commonly available in finite element codes for modeling delamination, and they have also been applied to the analysis of skin-stiffener separation. Like with any computational tool, however, the quality of the inputs has a significant effect on the quality of the results. Current practice using cohesive elements is to use fracture toughness properties characterized from damage initiation. Significant fracture behavior such as fiber bridging, however, often develops in fiber composite reinforced materials after initiation and as damage progresses beyond certain lengths. It is uncommon that damage progression data is collected during fracture characterization tests, and it is even rarer that properties characterized during damage propagation are used in analysis. Characterization of structural interface properties between a skin and stiffener, required as input for cohesive elements in finite element methods, is often more complex[3] than anticipated, especially when the skin and stiffener are made with two different materials and/or architectures. An example of such a structure is a skin panel made of a unidirectional tape composite

[1] Research Aerospace Engineer, Structural Mechanics and Concepts Branch, MS 190.
[2] Senior Research Aerospace Engineer, Durability, Damage Tolerance, and Reliability Branch, MS 188E.
[3] Research Aerospace Engineer, Analytical Mechanics Associates, MS 188E.

co-cured with a stiffener made of a fabric composite. While the fibers and matrix may (or may not) be the same material across the skin-stiffener interface, the architectural differences between the tape and fabric may lead to interface properties that are dependent on which direction a delamination propagates. Recent work[4] has indicated that interface properties may depend on the direction of the shear stress when the delamination propagates along the surface of the tape ply versus the surface of the fabric ply. Additionally, fracture toughness values for cracks propagating at dissimilar interfaces such as those between differing angled plies[5] or between tape and fabric materials have been shown to exhibit rising crack-growth resistance curve, or *R*-curve, effects. *R*-curve effects typically manifest as increasing fracture toughness with crack growth, followed by a plateau or steady-state.[6,7] The difference between the initiation values at an interface and the steady-state progression values may prove to be a deciding factor whether a skin-stiffener interface fails catastrophically without prior indication or whether the separation propagates gradually with an increasing applied load. Additionally, implementing varying fracture toughness properties from initiation-based to progression-based responses in a consistent approach is not well understood. The analytical work herein is an attempt to demonstrate the significance of *R*-curve effects on a structural scale and to expand on the idea of superposed bilinear cohesive laws[4,8] as a consistent method of best practice.

R-curve effects may be the result of many phenomena including, but not limited to, fiber bridging, crack-tip blunting, matrix microcracking, delamination migration, and crack ply delving.[9] In order to capture all of the possible contributions to *R*-curve effects, all relevant phenomena need to be included in a finite element model. Additionally, extremely high-fidelity models are required to accurately predict severe stress gradients across plies in matrix-rich layers, and even between individual fibers, as well as to predict matrix microcrack initiation and propagation. Such high-fidelity model refinement, though possible in theory, quickly exhausts practicality for many engineering uses. Therefore, a superposed cohesive law methodology[8] was implemented in this work to smear the small scale details of the micromechanics-level material failure events into a scale that is applicable and practical to structural-scale models. Previous work has shown that using two superposed bilinear cohesive laws can effectively create a trilinear cohesive law[4] that can capture the response of *R*-curve effects better than a single bilinear cohesive law.

In this work, a seven-point bend (7PB) test was used to collect data on stable skin-stiffener interface separation behavior. Skin-stiffener separations have been observed under compression along the stiffener direction and using a stiffener peel test. One disadvantage with skin-stiffener separation under axial compression is the often sudden and catastrophic failure, thereby making data collection during delamination initiation and propagation difficult. Alternatively, while damage may progress in a quasi-stable manner in the stiffener peel test, the test does not represent the stress states under in-use conditions or during damage progression such as compression leading to buckling. A significant advantage of the 7PB configuration is the quasi-stable damage initiation and progression in a deformation representative of a buckled configuration.[10] This configuration induces interlaminar normal and shear stresses that contribute to skin-stiffener separation.

Several experimental specimens were tested using the 7PB configuration, and numerous data were collected with which to investigate skin-stiffener separation. Experimental results were compared to predictions obtained from finite element models of the 7PB configuration. The finite element models were implemented with a range of skin-stiffener interface material properties. Section II describes the test specimen and experimental setup used to obtain data for comparison to the finite element model results. Section III describes the finite element model and the parameters that were varied in this study. The experimental and computational results are compared and discussed in Section IV. Section V provides a few concluding remarks and includes suggestions for future experimental and computational work.

II. Test Specimen and Experimental Setup Description

A. Experimental Test Specimens

The experimental results of three specimens were used in this study. The test specimens consisted of a flat panel skin with a single co-cured hat-shaped stiffener along the panel center, as shown in Figure 1. The hat-shaped stiffener was oriented along the 0-degree ply direction of the skin. The stiffener ran along the entire length of the specimen. The side of the specimen with the stiffener was called the *stiffener side* and the side without the stiffener was called the *skin side*.

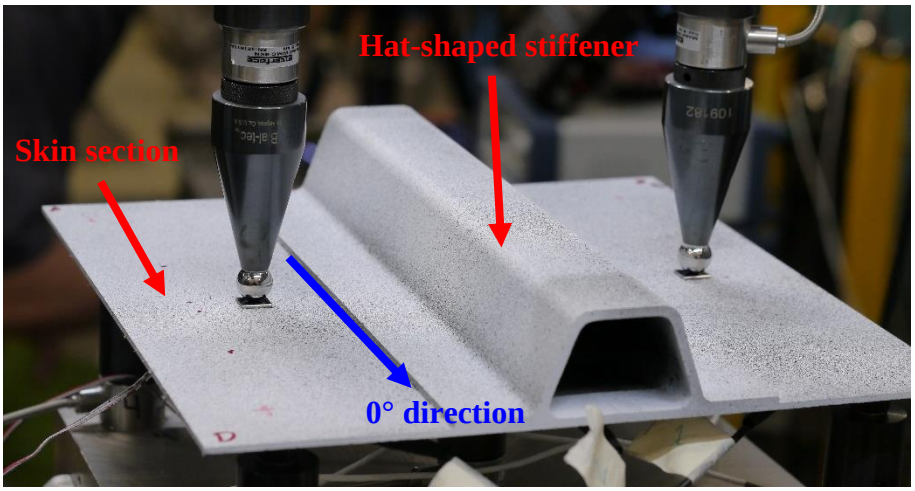

Figure 1. View of a seven-point bend test specimen looking at the stiffener side in an unloaded configuration.

The skin consisted of IM7-8552 unidirectional pre-impregnated carbon fiber epoxy matrix (pre-preg) tape with a stacking sequence of $[45/-45/0/90/45/-45/]_S$. The stiffener consisted of IM7-8552 plain weave fabric and was made of two separate sections. The first was a section wrapped around the interior mandrel that created the hat-shaped geometry, and the second section consisted of the flange and remaining stiffener overwrap plies. The interior wrap had a total of four plies with a stacking sequence of $[45/-45/0/45]_T$, and the overwrap had 12 plies with a stacking sequence of $[45/-45/0/45/45/0/-45/45/45/-45/0/45]_T$ where the last 45-degree ply of the interior wrap was adjacent to the first 45-degree ply of the overwrap. The ply stacking sequences for section interfaces are shown in Figure 2.

Panel dimensions were nominally 10 inches by 10 inches. The mean flange-to-flange width of the stiffener was 4.28 inches, and the mean width of the unstiffened skin section was 2.88 inches. The sum of these widths does not reconcile to exactly 10 inches due to tolerances in machining. The region in the corners at the intersections of the interior wrap, overwrap, and skin sections was filled with an adhesive material. This adhesive filled region is referred to in this work as a noodle.

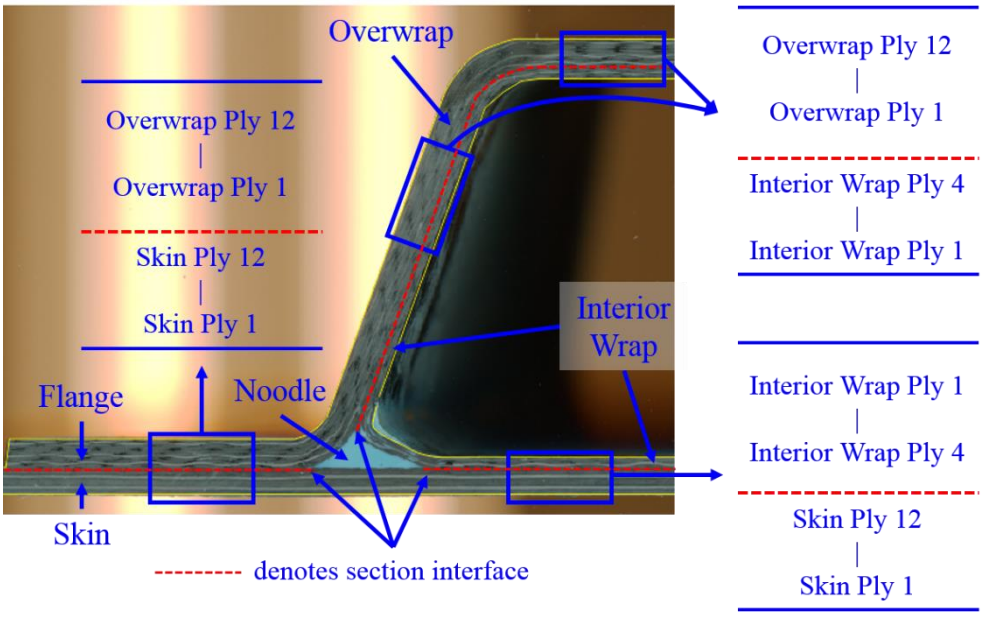

Figure 2. Partial stiffener cross-section view with ply stacking sequences of the skin, overwrap, and interior wrap sections.

The three specimens were cut from a larger "parent" panel. The parent panel was fabricated by The Boeing Company. The fabrication procedure started by placing the stiffener overwrap fabric plies in a stiffener mold. Then, a trapezoidal mandrel wrapped in the fabric interior plies was placed in the cavity of the stiffener. Pre-preg tape skin plies were then placed on top of the entire tool. The tool was then placed in an autoclave for curing. The mandrels were extracted after the curing cycle.

B. Seven-Point Bend Experimental Test Setup

The 7PB test fixture was configured with five lower supports and two upper load introduction points. Each support and load introduction point was implemented with a load cell for local load history data to be collected. All supports terminated in a hemispherical tip with a 0.5-inch diameter. An overview of the 7PB test fixture is shown in Figure 3.

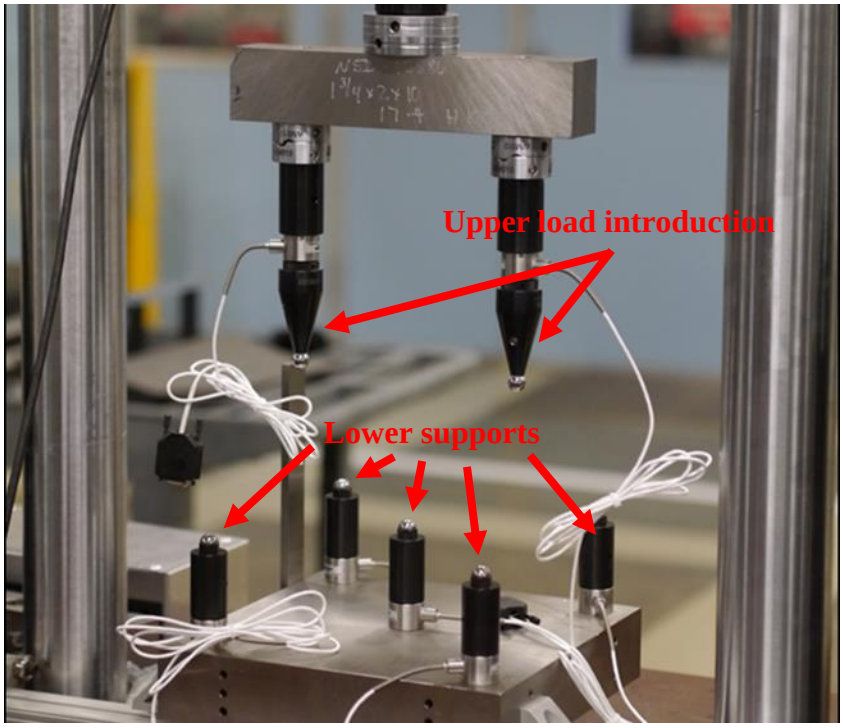

Figure 3. Overview of the seven-point bend test fixture with five lower supports and two upper load introduction points.

Washers were used as spacers between the lower hemispherical tips and the skin of the specimen. Square shims were used between the upper hemispherical tips and the skin of the specimen. The upper load introduction points were located symmetrically about the stiffener such that the deformation that is induced onto the specimen is similar to the buckled mode of a stiffened panel subjected to an in-plane axial compression load. The orientation of the specimen relative to the load introduction points is shown in Figure 1. A 7PB test specimen under load and deformed into a buckled-like configuration is shown in Figure 4.

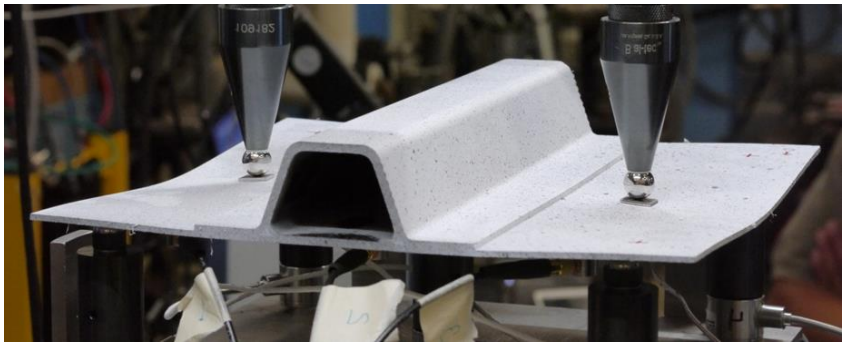

Figure 4. Example of a loaded seven-point bend test specimen deformed into a buckled-like configuration.

Loading was conducted under quasi-static displacement control on an Instron Model 1350 load frame. Each test setup had instrumentation for data collection during a load sequence. This instrumentation consisted of strain gages mounted to the skin of each specimen on the skin side, black and white speckle pattern for use of three-dimensional (3-D) digital image correlation (DIC) on the stiffener side, acoustic emission (AE) sensors, and thermal imaging cameras. Loading sequences were halted and the specimen unloaded after instrumentation, particularly the strain gages or the AE sensors, indicated initiation or progression of damage. After each load sequence, the test specimen was removed from the fixture and scanned using ultrasonic transmission (UT) and X-ray computed tomography (CT) techniques to characterize damage that initiated or progressed during loading. After completion of scanning, specimens were cycled through these steps multiple times gathering data on quasi-stable damage growth in a buckled-like deformation.

III. Finite Element Modeling Description

A. Shell Model

A finite element model of the 7PB test was created in MSC Patran using SC8R continuum shells. Continuum shells are general-purpose, finite-strain elements that may be used to model solid geometry unlike conventional shells which model a reference surface.[11] The analyses used the Abaqus/Standard 6.14-1 dynamic solver and the results were post-processed using Abaqus/CAE 6.14-1. The purpose of this model was to determine the feasibility of using continuum shells with cohesive elements to model interlaminar failure mechanisms to capture the response and failure events observed during the experiments. In this work, cohesive COH3D8 elements were used to model interlaminar failure between the skin and stiffener and were inserted between the stiffener flanges and the skin sections. The cohesive elements were placed in two regions about the centerline of the panel in 6-inch-long by 0.93-inch-wide rectangular zones, one on each side of the stiffener. The width of these rectangular zones corresponds to the width of the flange section in contact with the skin that does not include the noodle region. The location of the cohesive elements on both sides of the stiffener is shown in Figure 5.

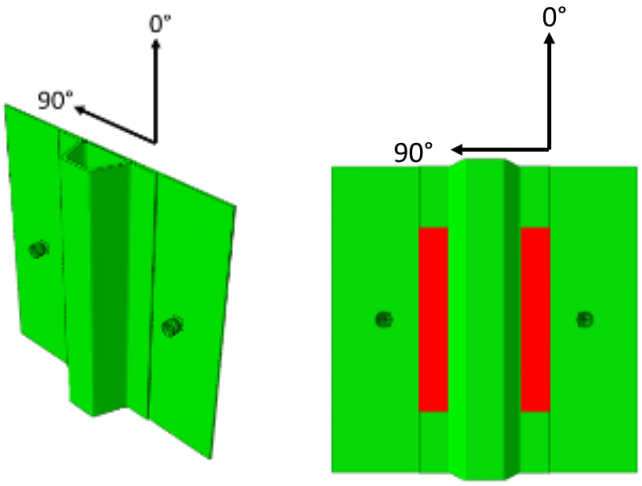

Figure 5. Perspective view of the seven-point bend shell model (left) with highlighted regions in red for location of the cohesive elements (right).

Both the skin and stiffener sections were modeled as composite laminates. Continuum shell elements, SC8R, were used for the skin and stiffener sections. One element through the thickness of the hat-stiffener overwrap and one element through the thickness of the interior wrap were used. Two-equally sized elements were used through the thickness of the skin, and the stacking sequence of the entire skin cross-section was split evenly between the two layers of elements. Square elements with edge lengths of 0.25-inch were meshed at the edges of the skin section, and the mesh gradually became more refined closer to the flange area. The skin elements were sized so the elastic response was not mesh dependent. The skin and flange elements were equally sized as the cohesive elements of 0.01-inch square. This refined mesh size, driven by the cohesive elements, was based on previous computational delamination studies. The noodle regions were modeled with continuum elements C3D8 and C3D6. A detailed view of the cross-section where the flange, noodle, wrap, and skin sections interface is provided in Figure 6. Linear elastic material properties were used for all sections of the skin, stiffener, noodles, and shims. Therefore, there was no damage under the load introduction points or the supports in any of the analyses as no damage was observed at those locations in the experiments.

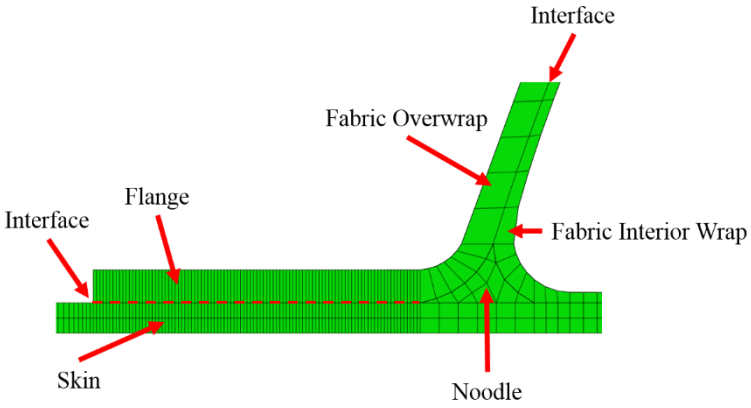

Figure 6. Partial stiffener cross-section with cohesive elements at the interface between the flange and skin shown as a dashed red line.

The interfaces between skin, stiffener, and noodle sections that did not have cohesive elements were either tied with tie constraints or were modeled with shared nodes and thus did not require tie constraints. No geometric or material imperfections were included in the analysis. The linear elastic material properties for the tape skin and fabric stiffener sections are provided in Table 1. Nominal specimen dimensions were considered. As such, comparison of analysis predictions to individual experimental results should be expected to show slight differences. Instead, predicting the general response of the experiments rather than specimen-specific behavior was the primary interest with the analyses.

Table 1 IM7-8552 tape and fabric material properties used in the shell model analysis

	E_1 (msi)	E_1 (msi)	ν	G_{12} (msi)	G_{13} (msi)	G_{23} (msi)	t (in.)
Tape	21.3	1.26	0.32	0.749	0.749	0.435	0.0072
Fabric	9.58	9.55	0.052	0.738	0.492	0.492	0.0078

B. Boundary and Loading Conditions

The lower 7PB supports and upper load introduction points were modeled as rigid hemispherical surfaces with a 0.5-inch diameter. Square shims between the load introduction points and the skin were modeled as elastic bodies. The shims were attached to the skin section using shared nodes. Frictionless contact between the hemispherical surfaces and the panel skin was implemented on the skin side and between the hemispherical surfaces and the shims on the stiffener side. The washers on the lower supports were not modeled as they did not affect the deformation of the panel but did prevent damage from occurring in the experiment. The first step in the analysis consisted of a thermal analysis that represented the effect of the cool-down after curing on residual deformation and stresses. No mechanical loads were applied during this step. At the end of the step, the locations of the five lower supports, which were held in contact with the skin using spring elements, were held fixed in place. During the second step, the two upper load introduction points were assigned translational displacement towards the skin to represent displacement control applied during the experiments. All other rotational and in-plane translational degrees of freedom were constrained in the upper load introduction points. Due to the large out-of-plane displacement response of the specimen, geometrically nonlinear analysis was used.

C. Representing Skin-Stiffener Interfaces with Cohesive Zone Models

The fracture toughness, or energy release rate G_c, is the most important material property to characterize the resistance to separation. Several standard tests are used to measure G_c for delamination in modes I, mode II, and mixed mode. These tests are conducted using unidirectional specimens, and the value of G_c is measured at the initiation of delamination propagation. However, the fracture toughness values obtained from these standard interlaminar fracture characterization tests may not account for the complex behavior of multiple damage phenomena contributing to delamination crack-growth resistance that occurs in real structures, where combinations of fiber bridging, delamination migration, interactions between transverse matrix cracks and delaminations accumulate in the wake of the delamination front. These mechanisms blunt the delamination fronts and can increase the fracture toughness by a factor of four or more compared to the initiation values.[5] This progressive increase in fracture resistance with crack growth is referred to as the *R*-curve.

It has been shown that a wide range of *R*-curves can be represented using dual superposed bilinear cohesive laws.[8] The effective result of the superposed dual bilinear cohesive laws is a trilinear cohesive law as represented in Figure 7. The first cohesive law, shown in red, represents the standard interlaminar properties at delamination initiation. The second cohesive law, shown in blue, accounts for the increase in resistance with crack propagation. Representing complex damage mechanisms with a cohesive law is a simple way to avoid the computational cost and complexity associated with high-fidelity finite element models.

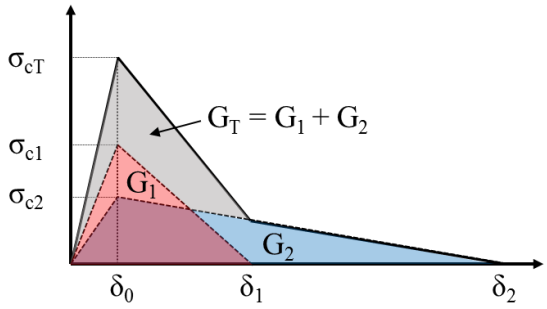

Figure 7. Superposition of two bilinear laws effectively resulting in trilinear law behavior.

In the following sections, analyses were performed using three combinations of the material properties reported in Table 2. The first solution consists of using a single cohesive law with initiation values of G_c. The corresponding properties are shown in Table 2 as *Cohesive Base*. Using these base properties is the current standard practice in industry. The second solution superposes the Cohesive Base properties and *Tape-Fabric Bridging* properties, which were obtained by fracture toughness characterization of the tape-fabric interface in IM7-8552 laminates.[9] The last solution consists of the superposition of Cohesive Base properties and *Structural Bridging* properties. The Structural Bridging properties represent an increase in crack resistance over the Tape-Fabric Bridging properties to represent interface separations that are characterized by extensive interactions of damage modes. The Structural Bridging properties were obtained by testing three-point bend specimens.[4] The material property inputs for the three cohesive laws used in the analyses are reported in Table 2.[4]

Table 2 Cohesive zone material properties used for the base law and superposed bridging law

	K_I (lb/in^3)	K_{sh} (lb/in^3)	G_{IC} (lb/in)	G_{IIC} (lb/in)	σ_C (lb/in^2)	τ_C (lb/in^2)	η_{BK}
Cohesive Base	1.8E+8	1.3E+8	1.37	4.22	9.040E+3	1.349E+4	2.07
Tape-Fabric Bridging	2.0E+7	3.0E+7	2.0	12.0	1.0E+3	3.0E+3	3.0
Structural Bridging	1.0E+7	1.5E+7	3.0	16.0	5.0E+2	1.5E+3	3.0

IV. Experimental and Numerical Results and Discussion

Three tests specimens were used in this study to compare with the finite element analysis predictions. The specimens were labeled as 7PB-010, 7PB-011, and 7PB-012. For brevity, they will be referred to simply as panels 10, 11, and 12 herein. Panel 10 was loaded a total of five times, with moderate damage observed under each flange at the termination of the last load sequence. Panel 11 was loaded only three times. The last load sequence for panel 11 was carried well beyond initial AE, thermography, and strain gage indications of damage progression and taken to the highest load of all load sequences for all three test articles. Loading was taken to this level so that at least one panel would have significant amounts of damage observed under the flanges. Panel 12 was loaded a total of four times. UT scans indicated that delamination may have halted at the region under the noodle section, which suggests the adhesive-filled region may influence propagation beyond the area under the flange. Additional investigation using higher-fidelity CT scans would clarify the extent of the delamination growth.

A consistent loading history was observed across all five load sequences of panel 10. A slightly increased bending stiffness was observed in run 2, relative to the other runs, where misalignment of the specimen in the test fixture is suspected. The first run was terminated at 791 lb after indications from AE sensors. However, minimal delamination was observed from the UT scan data. Runs 2 and 3 were terminated at a slightly lower load level than the load reached in run 1, at 784 lb and 789 lb, respectively, but the panel response was different in those two runs. In particular, UT data obtained after run 2 indicated that most of the delamination developed on one side of the specimen with some, but relatively small, delamination under the opposite flange. Run 3 was terminated at a load level between the levels reached in runs 1 and 2, and UT scan data indicated that most of the delamination progression occurred under the flange that had minimal damage at the end of run 2. After run 3, delamination remained fairly even under both flanges

as damage progressed. Runs 4 and 5 were terminated at 892 lb and 959 lb, respectively. The experimental load-displacement response for panel 10 and the corresponding finite element model predictions are shown in Figure 8. UT scans obtained after runs 1-5 are shown as the gray and black images, and the analytical predictions for the flange region are shown as the red and blue images. The shell components of the model are removed to view the damaging cohesive elements. The red areas in the model contours represent elements that have completely progressed through the softening portion of the traction separation constitutive law, indicating delamination, and are completely failed. The predicted results are scaled in size that is consistent with the measured UT results.

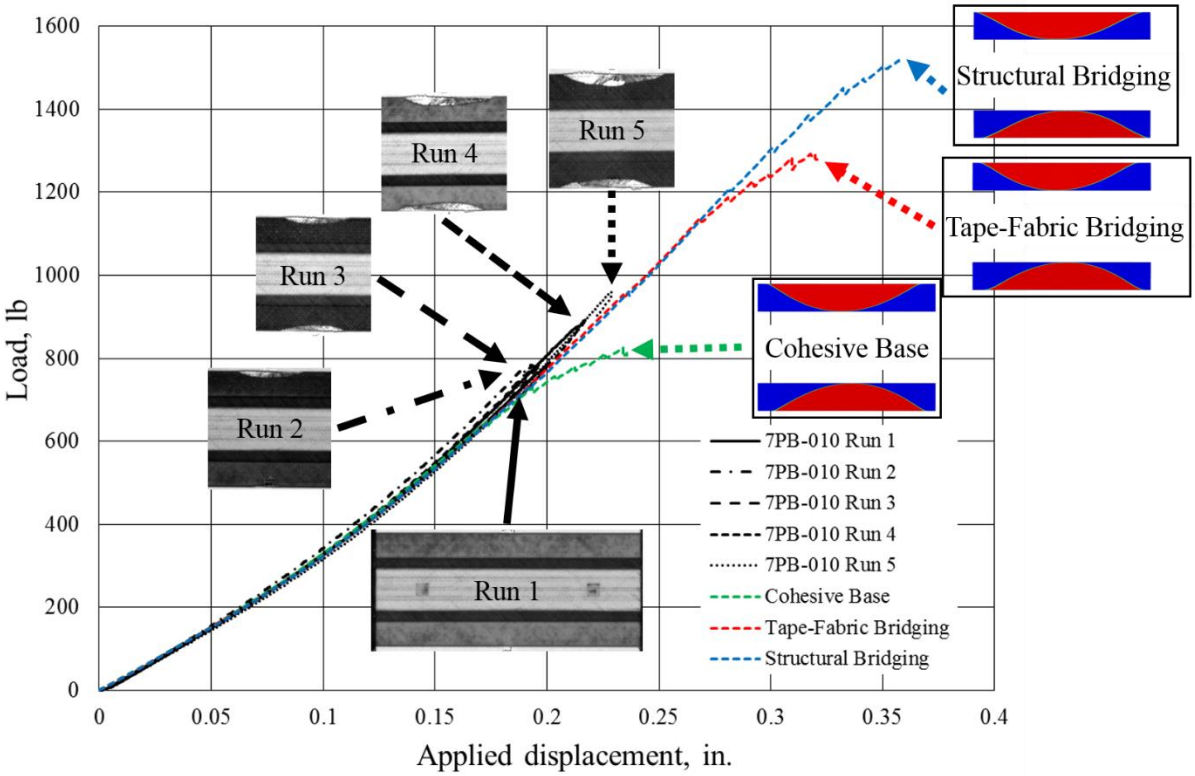

Figure 8. Load-displacement data for panel 10 and finite element models showing delamination state at the termination of each run.

The predicted load-displacement response obtained with the tape-only single cohesive law, Cohesive Base shown in green dashed line, agreed well with the initial linear response of panel 10. Upon delamination initiation, however, the structural stiffness quickly dropped below what was observed experimentally. Delamination progression in the cohesive layer was also extensive at lower loads when compared to experimentally observed delamination growth. The predicted load-displacement response obtained with the Tape-Fabric Bridging and Structural Bridging models, shown in red and blue dashed lines, respectively, agreed well with the initial response of panel 10. The load-displacement data for the models was terminated when the delamination front was a single element away from the boundary of the cohesive zone. Delamination observed via UT inspection of the panel and predicted delamination contours from the cohesive elements at equivalent displacements are shown in Figure 9. The values of the load are also provided for comparison since each point of comparison is at similar displacement. Different shades of grey in the UT scan images indicate delamination damage had developed on multiple interfaces of the skin in addition to the skin-flange interface.

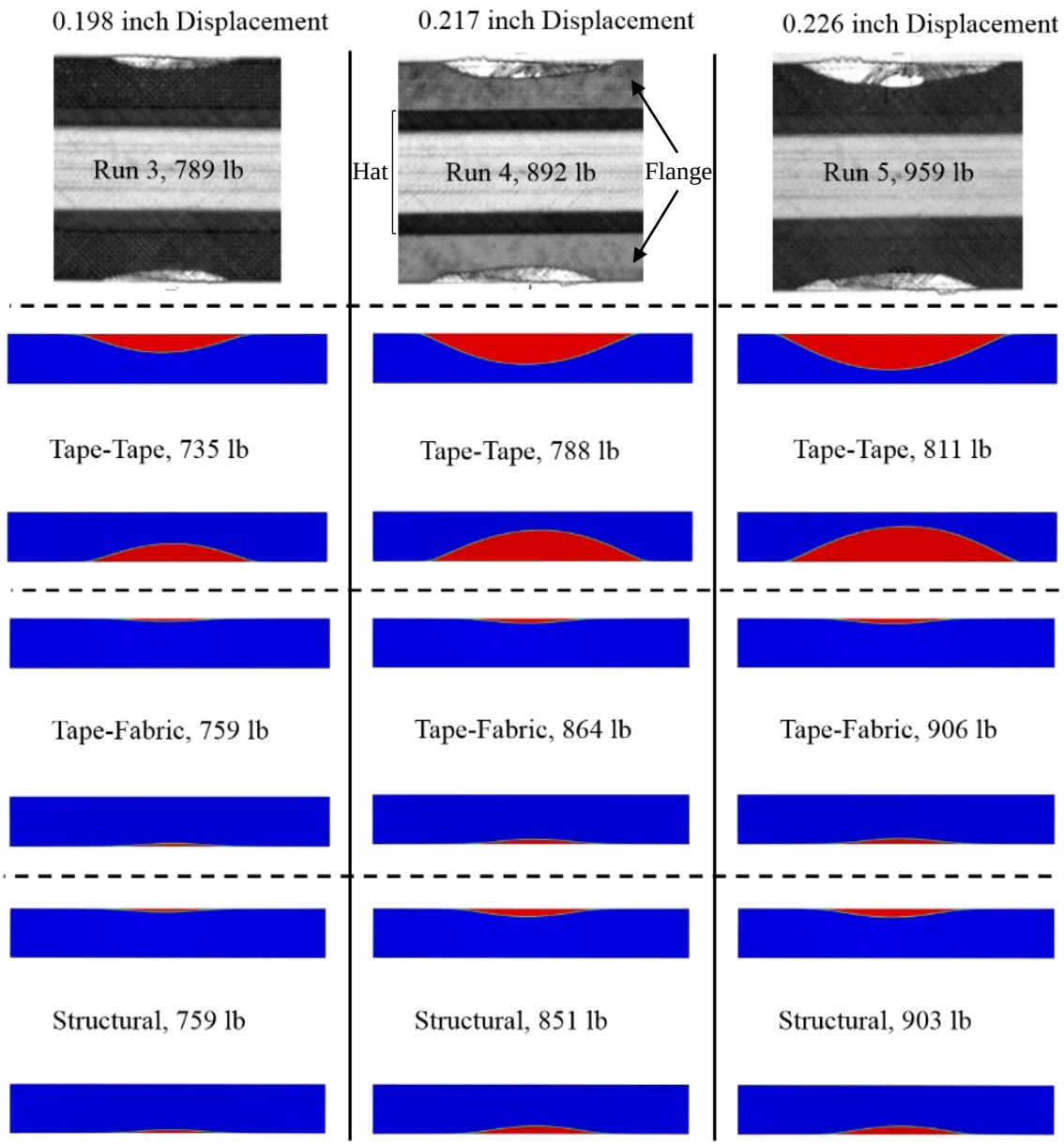

Figure 9. Diagram comparing panel 10 ultrasonic scans of delaminations to predicted delaminations at displacements where tests were terminated.

A consistent loading history was observed across all three runs of panel 11. Different delamination behavior was observed in panel 11 compared to panel 10 in that delamination was initially asymmetric as it developed under only one of the two flanges. Delamination initiation was first indicated near 846 lb. In run 2, the panel was loaded to a higher load of 1,024 lb. UT scans obtained after run 2 showed propagation of the delamination under one flange and no delamination under the opposite flange. In run 3, loading was carried well beyond additional damage growth indications from AE, thermography and strain gages, and was ultimately halted at 1,294 lb. Extensive symmetric delamination under the flanges was observed in the UT scans obtained after run 3. Different shades of grey in the UT scan image indicate delamination damage had developed on multiple interfaces of the skin in addition to at the skin-flange interface. In addition, this was the first test where delamination was shown to extend to the area of the noodle. It is not clear whether the delamination grew under or over the noodle. The load-displacement response for panel 11

and the corresponding predicted response are shown in Figure 10. UT scans obtained after runs 1-3 and predicted failed cohesive law elements with the shell elements removed are included as callouts.

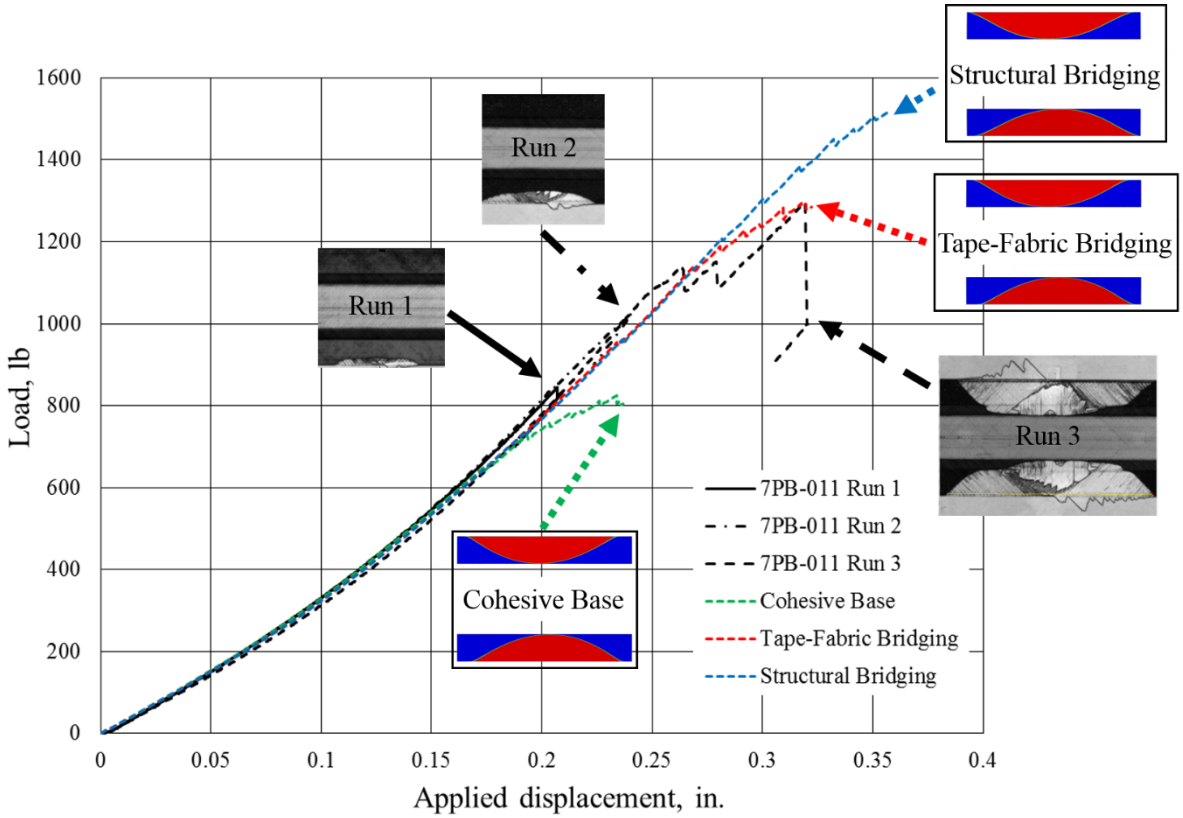

Figure 10. Load-displacement data for panel 11 and finite element models showing delamination state at the termination of each run.

Predictions from the Cohesive Base law significantly deviated from experiments as the load exceeded 600 lb. The predicted load-displacement response obtained with the Tape-Fabric Bridging and Structural Bridging models agreed well with the initial response of panel 11. Deviation in agreement in the load-displacement response occurred at higher loads as the damage state in the test specimens deviated from what was predicted by the models. Runs 1 and 2 were terminated at an asymmetric delamination state. Note that the exhaustion of the Tape-Fabric Bridging model cohesive element corresponds to a load and displacement at which significant load drop was observed in the test. The delamination contours obtained from UT inspection at the termination of each run and the delamination contours and loads of each model at equivalent displacements are shown in Figure 11.

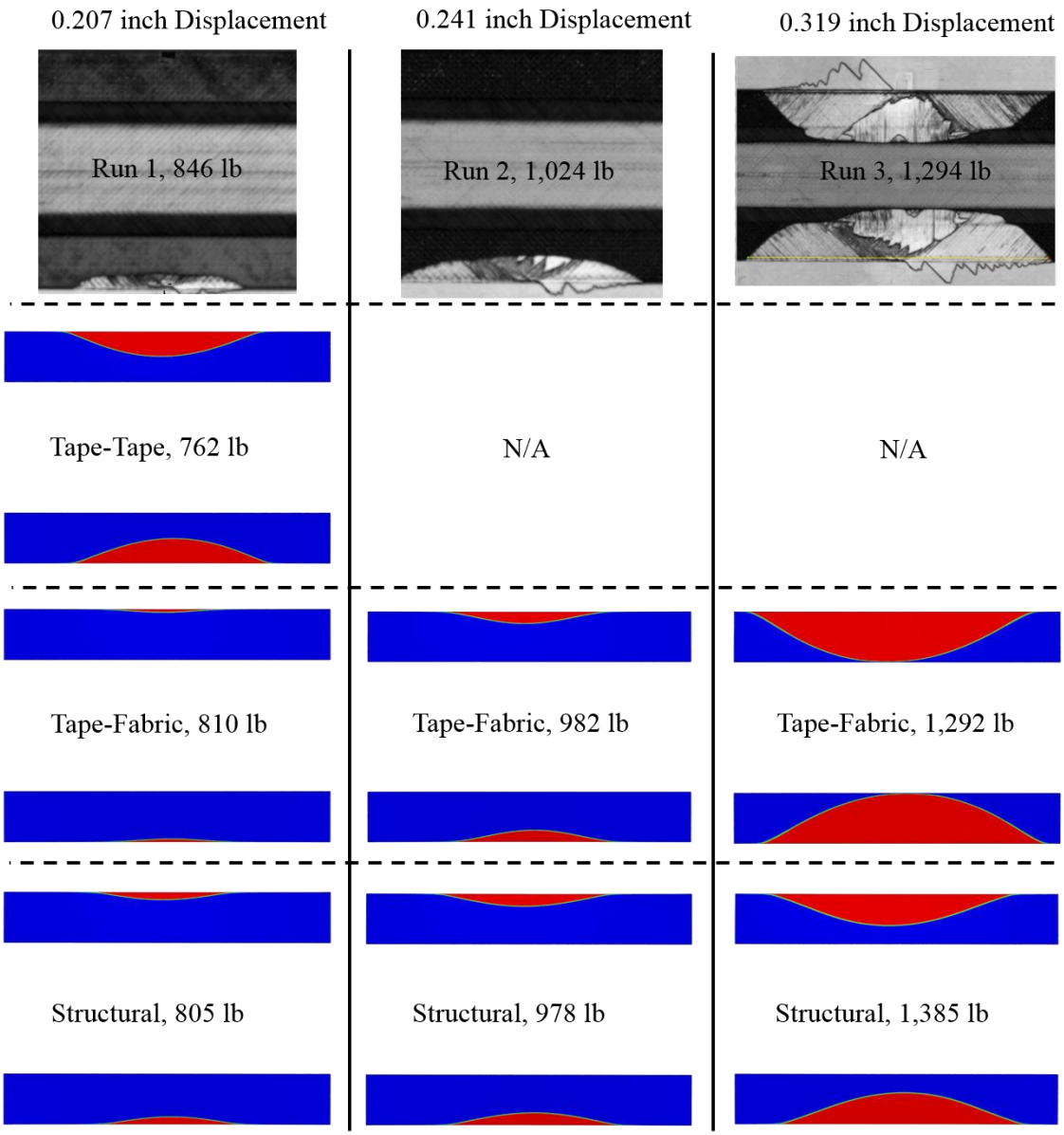

Figure 11. Diagram comparing panel 11 ultrasonic scans of delaminations to predicted delaminations at displacements where tests were terminated.

Panel 12 load sequences, aside from run 3, also showed consistent loading history between each run. The panel response in run 3 was uncharacteristic when compared to the response observed in all other sequences, and the deviation in behavior was possibly due to specimen misalignment within the load fixture. Results of panel 12 run 3 were not considered when comparisons to model results were made but are provided for complete loading and damage history. Acoustic emission sensors indicated onset of damage at 804 lb in run 1, yet no delamination damage was observed in the post-test UT scan. Run 2 was terminated at a lower load of 772 lb and delamination was observed under one flange. In run 3 the panel was loaded significantly higher and showed inconsistent load-displacement response. Run 3 was terminated at 1,126 lb, at which point delamination had not initiated under the other flange. Run 4 was terminated at 1,079 lb and delamination was observed under both flanges. The area of delamination under the second flange was extensive and corresponded to the significant load drop recorded in run 4. The load-displacement response for panel 12 and the corresponding finite-element predictions are shown in Figure 12. UT scans obtained after runs 1-4 and exhausted cohesive law elements with the shell elements removed are included as callouts.

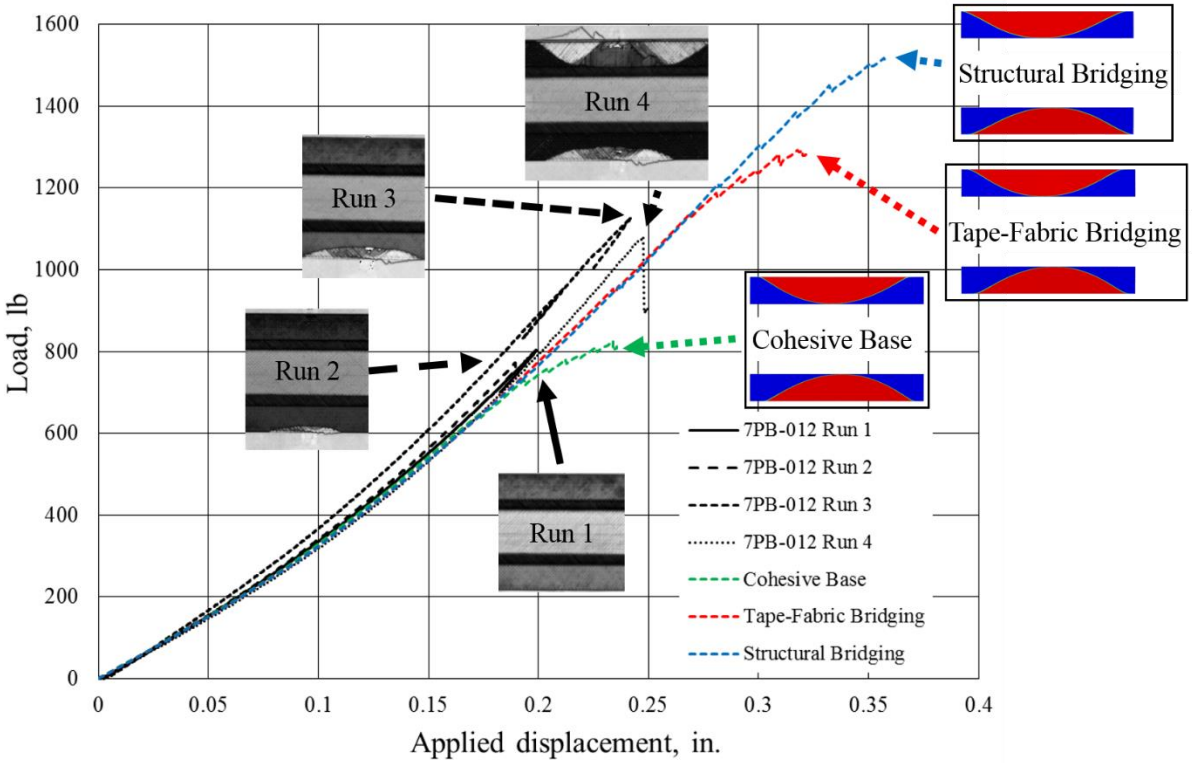

Figure 12. Load-displacement data for panel 12 and finite-element models showing delamination state at the termination of each run.

The predicted panel response did not correlate well with the experimental results for panel 12 because of the lack of symmetry in the observed delaminations. In addition, the sudden and unstable delamination growth was not captured well in the models. The delamination areas measured after run 4 were much larger than those predicted by both analysis models. It was interesting to note, however, that the bridging models analysis nearly bisected the loads just prior to and post unstable delamination growth. This may suggest that the smeared behavior of the cohesive laws is applicable while not capturing individual failure event instability. UT scans and exhausted delamination zones for panel 12 at approximately equal displacements are provided in Figure 13.

Analysis predictions from the bridging models slightly under-predicted the experimental reaction force across all specimens. The Cohesive Base model significantly under-predicted the experimental reaction forced after delamination initiation. This difference indicated that the as-built models were slightly more compliant than the test specimens. The area of the delaminations observed experimentally was also under predicted for the bridging models at similar displacements. The delamination contours in all models were predicted to grow in a stable manner with slight load drops associated with increased rate of delamination propagation. In the tests, however, the delamination initiation and growth behavior was slightly less stable. This so-called “stick-slip” behavior has been observed in other work and has been difficult to capture numerically.

The cohesive base and the bridging models have bound the range of experimentally observed responses. While the cohesive base model significantly under-predicted the experimental reaction force and stiffness after delamination initiation, the predicted rate at which delamination propagated may be closer to the experimental propagation rate than the predicted by bridging models. Conversely, the bridging models maintained stiffness after delamination initiation but tended to suffer from slower delamination growth than observed in the experiments. This may suggest the process zone of the bridging law is tougher in the analysis than the experiments. By providing a lower bound with a tape-only model and an upper bound with the superposed bridging laws, a set of cohesive laws should exist that captures the onset of delamination, maintained structural stiffness response, and slightly increased delamination growth rates compared to the sets provided in Table 2.

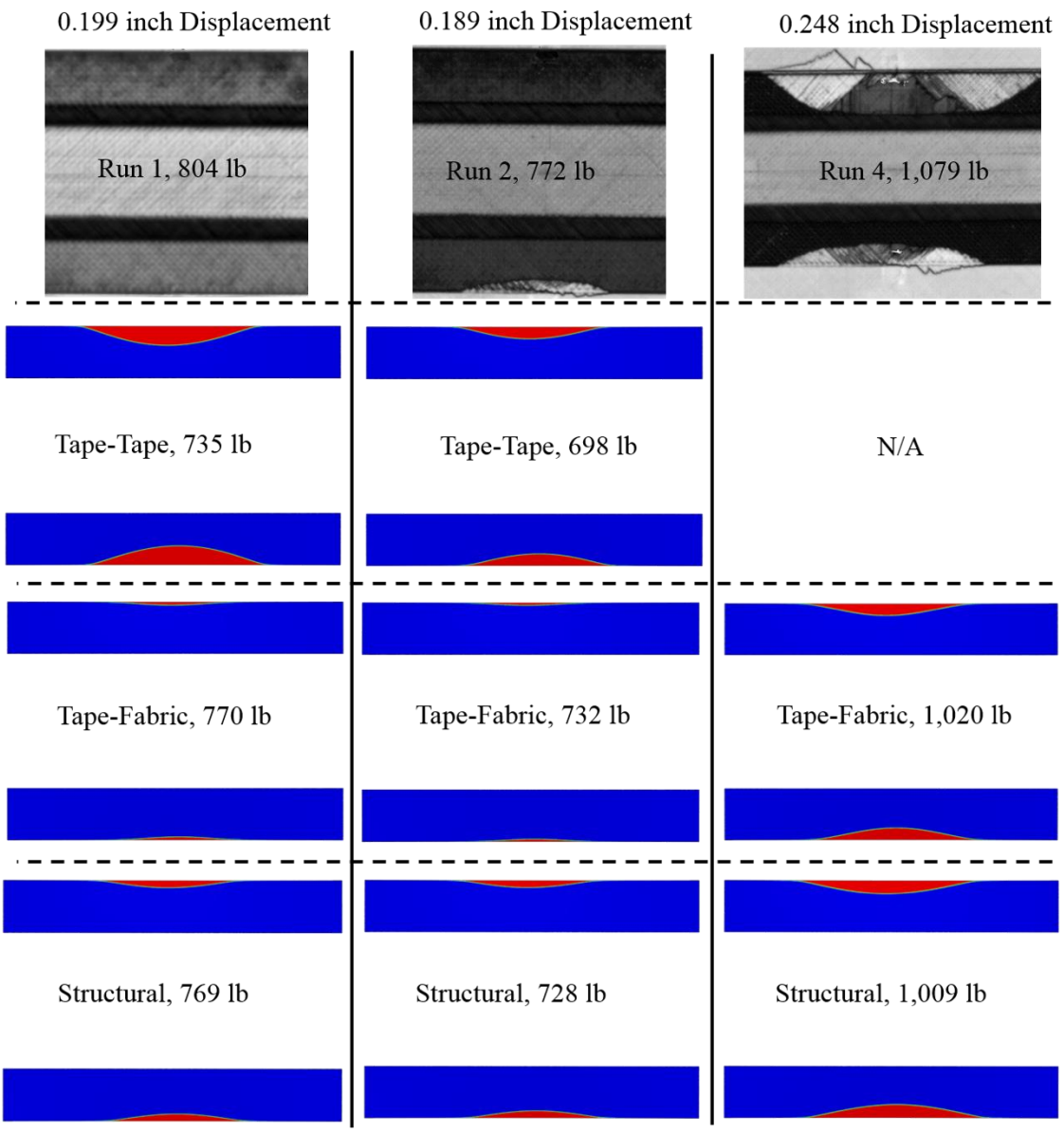

Figure 13. Diagram comparing panel 12 ultrasonic scans of delaminations to predicted delaminations at displacements where tests were terminated.

V. Concluding Remarks

Stiffener separation has garnered significant attention in the aerospace community as many interacting failure modes like matrix microcracking, delamination migration, multiple delamination initiation locations, and fiber failure combine to challenge current understanding of advanced composite failure mechanisms. Widespread use of advanced carbon fiber reinforced polymer composites in stiffened structures increases the need for deeper understanding of the underlying fundamental mechanisms that contribute to failure events such as stiffener separation. Cohesive elements have become one commonly available feature in analysis methods to model skin-stiffener separation. The standard practice of using a single cohesive law, with properties from damage initiation alone, however, may not be sufficient to accurately predict skin-stiffener separation. Delamination propagation at dissimilar interfaces, such as those between differing angled plies or between tape and fabric materials, can exhibit significant *R*-curve effects. In order to capture all of the possible contributions to *R*-curve effects, many phenomena need to be included in a finite element

model. This work implemented a dual bilinear cohesive law methodology to smear details of the micromechanics level material failure events into a scale that is tractable at the structural scale.

A seven-point bend (7PB) test was used to collect data on stable skin-stiffener interface separation behavior. Several experimental specimens were tested using the 7PB configuration. Experimental results were compared to finite element analysis predictions of the 7PB configuration. The finite element models were implemented with a range of skin-stiffener interface material properties. The first analysis used a single cohesive law with initiation values of G_c. Two additional analyses were conducted using superposed bilinear cohesive laws to represent different *R*-curves determined from tests previously conducted. Results from the first analysis indicated that damage growth was over-predicted compared to results obtained experimentally, and the specimen stiffness was significantly under-predicted after damage initiation. Using the superposed cohesive laws in the analysis increased the accuracy of the predicted response. However, analysis conducted with the superposed cohesive laws under-predicted the extent of delamination compared to the experimentally measured damage at equivalent displacement. In addition, experimental results indicated that there was a "stick-slip" phenomenon representative of potentially unstable delamination growth that was not well captured in the analysis. Development of a global-local model, with the local model able to capture more discrete failure details, will be pursued as future work.

Acknowledgments

This work was funded as part of the Advanced Composites Project. The authors thank The Boeing Company for manufacturing the test specimens used in this work. They also extend gratitude and thanks to those who assisted the testing setup, data collection, and data reduction.

References

[1] Krueger, R., Cvitkovich, M. K., O'Brien, T. K., and Minguet, P. J., "Testing and Analysis of Composite Skin/Stringer Debonding Under Multi-Axial Loading," NASA TM-209097, February, 1999.

[2] Rose, C. A., Dávila, C. G., and Leone, F. A., "Analysis Methods for Progressive Damage of Composite Structures," NASA TM-218024, July, 2013.

[3] Ratcliffe, J. G., and Johnston, Jr., W. M., "Influence of Mixed Mode I-Mode II Loading on Fatigue Delamination Growth Characteristics of a Graphite Epoxy Tape Laminate," *29th American Society for Composites Technical Conference*, La Jolla, CA, 2014.

[4] Dávila, C. G., Leone, F. A., Song, K., Ratcliffe, J. G., and Rose, C. A., "Material Characterization for the Analysis of Skin/Stiffener Separation," 32nd *American Society for Composites Technical Conference*, West Lafayette, IN, 2017.

[5] Pereira, A. B., and de Morais, A. B., "Mode I Interlaminar Fracture of Carbon/Epoxy Multidirectional Laminates," *Compos. Sci. Technol.*, vol. 64, no. 13–14, pp. 2261–2270, 2004.

[6] Sørensen, B. F., and Jacobsen, T. K., "Large-Scale Bridging in Composites: R-Curves and Bridging Laws," *Compos. Part A*, vol. 29, no. 11, pp. 1443–1451, 1998.

[7] Czabaj, M. W., and Ratcliffe, J. G., "Comparison of Intralaminar and Interlaminar Mode I Fracture Toughnesses of a Unidirectional IM7/8552 Carbon/Epoxy Composite," *Compos. Sci. Technol.*, vol. 89, pp. 15–23, 2013.

[8] Dávila, C. G., Rose, C. A., and Camanho, P. P., "A Procedure for Superposing Linear Cohesive Laws to Represent Multiple Damage Mechanisms in the Fracture of Composites," *Int. J. Fract.*, vol. 158, no. 2, pp. 211–223, 2009.

[9] Ratcliffe, J. G., Czabaj, M. W., and O'Brien, T. K., "A Test for Characterizing Delamination Migration in Carbon/Epoxy Tape Laminates," NASA TM-218289, August, 2014.

[10] Bertolini, J., Castanié, B., Barrau, J. J., Navarro, J. P., and Petiot, C., "Multi-Level Experimental and Numerical Analysis of Composite Stiffener Debonding. Part 2: Element and Panel Level," *Compos. Struct.*, vol. 90, no. 4, pp. 392–403, 2009.

[11] Abaqus 6.14 Online Documentation, Dassault Systémes, Providence, RI, 2014.